NIPER-485
Distribution Category UC-122

# IMAGING TECHNIQUES APPLIED TO THE STUDY OF FLUIDS IN POROUS MEDIA

Topical Report

NIPER--485

DE91 002215

By
Liviu Tomutsa
D. Doughty
S. Mahmood
A. Brinkmeyer
M. P. Madden

January 1991

Work Performed Under Cooperative Agreement No. DE-FC22-83FE60149

Prepared for
U.S. Department of Energy
Assistant Secretary for Fossil Energy

Robert Lemmon, Project Manager
Bartlesville Project Office
P.O. Box 1398
Bartlesville, OK 74005

Prepared by
IIT Research Institute
National Institute for Petroleum and Energy Research
P.O. Box 2128
Bartlesville, OK 74005

TABLE OF CONTENTS



TABLES



ILLUSTRATIONS

# IMAGING TECHNIQUES APPLIED TO THE STUDY OF FLUIDS IN POROUS MEDIA

By L. Tomutsa, D. Doughty, S. Mahmood, A. Brinkmeyer, M. P. Madden

## ABSTRACT

The dynamics of fluid flow and trapping phenomena in porous media was investigated using a number of rock-fluid imaging techniques. Miscible and immiscible displacement experiments in heterogeneous Berea and Shannon sandstone samples were monitored using X-ray computed tomography (CT scanning) to determine the effect of heterogeneities on fluid flow and trapping. Thin sections were cut from these sandstone samples from areas exhibiting different flow and trapping characteristics. The statistical analysis of pore and pore throat sizes in these thin sections enabled the delineation of small-scale spatial distributions of porosity and permeability. Multiphase displacement experiments were conducted with micromodels constructed using thin slabs of the sandstones. The combination of the CT scanning, thin section, and micromodel techniques enables the investigation of how variations in pore characteristics influence fluid front advancement, fluid distributions, and fluid trapping. Plugs cut from the sandstone samples were investigated using high resolution nuclear magnetic resonance imaging (NMRI). NMRI permitted the visualization of oil, water or both within individual pores. The integration of results at different scales using these imaging techniques will advance the understanding of how small-scale rock heterogeneities influence fluid flow and trapping. The application of these insights will aid in the proper interpretation of relative permeability, capillary pressure, and electrical resistivity data obtained from whole core studies.

## INTRODUCTION

A detailed understanding of rock structure and its influence on fluid entrapment, storage capacity, and flow behavior can improve the effective utilization and design of methods to increase the recovery of oil and gas from petroleum reservoirs. Knowledge of the interrelationships between measurements at pore to whole-core scales is necessary for accurate evaluation of core property measurement techniques. Direct visual examination of pore-space geometry and fluid distributions among pores and at the whole core level is important to assist in understanding mechanisms controlling fluid flow and trapping within reservoir rock. Such observations enable the construction of realistic mathematical models to predict the effect of heterogeneity on fluid flow. More accurate predictions of fluid flow will increase the utility and reliability of oil production predictions using numerical simulators.

Pore-level measurements can be facilitated by the use of computer-assisted image analysis of thin sections and micromodel observations. Thin section and micromodel techniques rely on optical

microscopy to obtain images at a useful resolution of between 1 and 50 μm. Images of thin sections yield geometric data about pore structure. Observations of fluids in micromodels help to generate an understanding of multiphase fluid flow in porous media. Core-scale measurements of the spatial distributions of rock properties and the advancement of fluid fronts can be performed using X-ray computed tomography (CT scanning) and nuclear magnetic resonance imaging (NMRI). These methods recently have emerged as powerful, nondestructive, noninvasive investigative techniques. The useful resolution of CT scanning ranges between 500 and 1,000 μm, while that for NMRI ranges between 20 and 1,000 μm. At these resolutions, CT scanning and NMRI are ideal tools for studying average properties over a small number of pores (see figure 1).

During previous years, the main effort on this and related NIPER projects was directed toward establishing an image analysis laboratory. Various imaging techniques were integrated with a full-color, real-time image analysis system with the capability of measuring lengths, areas, angles, and pixel intensities on features defined by the operator. Improved methods of constructing thin rock-slab micromodels and an appropriate optical observation system were developed. An NMRI apparatus was constructed from an analytical NMR unit, and improved magnetic field gradient coils were designed and constructed to improve NMRI resolution. Finally, a third-generation CT scanner was installed in the image laboratory. The location of all these various rock-fluid imaging facilities within a single laboratory and the integration of information obtained from them provide a unique opportunity to investigate rock features from the pore to the core scale and to develop a clearer understanding of the factors that influence fluid flow and trapping in reservoir rock. The concept of integrating various imaging techniques is illustrated in figure 2.

The objectives of the project are to develop and use new imaging techniques for measurements of pore geometries and fluid distributions in reservoir rocks at scales varying from pore level to whole core level and to study the effect of microscopic-scale rock heterogeneities on oil trapping in core-size rock samples. The first task of the project specified that the NIPER CT scanner would be adapted for measurements of the spatial distributions of two-phase fluid saturations. The results of this task are presented in the sections on CT hardware, porosity and saturation calculations, and measurement of fluid distribution by CT scanning. The second task, which followed closely from the first, called for the measurement of single- and two-phase spatial fluid distributions in large core plugs. The results are presented in the sections on measurement of single- and two-phase fluid distribution, coreflood results, nuclear magnetic resonance imaging developments, and experimental results and discussion from NMRI imaging studies. The results of the third task, related to the use of micromodels, are presented in the section on micromodel study of pore-level fluid distributions. Finally, the results of the fourth task to

correlate pore geometry to fluid distribution in porous media are presented in various sections that describe specific imaging techniques.

Work on rock-fluid imaging will continue next year. Objectives are to continue improvement of the methodologies to derive reservoir engineering parameters from petrographic, CT scanning, and NMR images; to apply state-of-the-art technology to support efforts directed to improving oil recovery from high-priority reservoirs; and to transfer newly developed technology to the petroleum industry.

## CT SCANNING

### Hardware

A Siemens Somatom II computed tomography (CT) scanner has been used to obtain images of cores with and without fluid flow processes. The scans were taken mostly on the high-resolution mode at 125 kV and 460 mAs. The CT can also use 96 kV and 115, 230 and 300 mAs. A scan takes 5 seconds in the medium-resolution mode and 10 seconds in high-resolution mode. The generated image is stored on the CT computer hard disk temporary storage. At present, as many as 64 images can be stored in temporary storage. By replacing the diskpack, as many images as needed can be stored rapidly and retrieved for investigation later. Images can also be stored on floppy disks. The stored images can be retrieved for processing on the CT computer or an image processing microcomputer. The following algorithms are available: zooming, image addition and subtraction, histogram of CT density values within a region of interest, average CT density in a circle of specified radius and center location, CT density profile along any direction, and distance and angle measurements. Images are automatically annotated with title information, date of scan, image number, thickness of section, exposure time, X-ray tube kV, and sample position with regard to a zero point established at the start of the scanning operation. A Polaroid camera provides instant high quality 4 in. by 3 in. photos on special low-contrast black and white Polaroid film. The scanner has a conveyor belt table, the movement of which can be controlled from the console in steps as small as 1 mm. The position of the table is read to 1 mm precision. A fastening device which uses the CT gantry alignment lights was constructed for accurate and reproducible positioning of the coreholder.

A low-pressure (< 200 psi) coreflooding experimental setup has been installed in the CT room. It allows the control and monitoring of fluid inlet pressures and rates and fluid production rates without interfering with CT scanning. Both constant pressure and constant rate flood experiments can be performed. Positioning devices for both epoxied slabs (10 cm x 5 cm x 2 cm) and low-pressure coreholders for 2-in. diameter cores (up to 8 in. long) have been designed and built. They allow CT scanning along the direction of flow with a minimum of artifacts.

Because of beam hardening, an attenuation cupping effect takes place when scanning rock samples, with the X-ray attenuation increasing from the center toward the periphery of the samples. By surrounding the sample with attenuating materials (tagged fluids, sand, rock) such that the shape of the entire volume scanned approaches cylindrical symmetry, the cupping is reduced; however, the noise present in the image is increased due to the weakening of the X-ray beam reaching the detectors. This causes an uncertainty in the values of the attenuation for each image voxel. The average voxel uncertainty was obtained by subtracting images taken of the same sample. Because the odd and even scans are taken by the movement of the gantry in opposite directions and a certain slack is present in the mechanical drive, two consecutive images are slightly displaced. Thus, for avoiding errors due to this slight misalignment, odd images were subtracted from odd images and even from even. An average voxel uncertainty of 5 Houndsfield units was obtained. For a brine tagged with 20% NaI, in a 30% porosity rock, this value corresponds to a 2.5% uncertainty in the saturations computed from CT images. By recalibrating the CT scanner for the higher density present in quartz and with improvements in the selection of the attenuating materials surrounding the core, it is expected to reduce this number further.

## Porosity and Saturation Calculations

Each CT image is a visual representation of the X-ray attenuation of each of the 256 x 256 volume elements (voxels) present in the selected object slice. Each voxel represents a rectangular volume with sides of a minimum of 0.5 mm x 0.5 mm and height of 2, 6, or 8 mm depending on the slice thickness selected. The X-ray attenuation is expressed in CT density units which use the Houndsfield unit definition with air at -1,000, water at 0, and the cores in the 1,200 to 2,000 range. A linear relationship exists between the CT attenuation and the amount of the attenuating material present in the voxel measured. This linearity has been verified for this CT scanner as shown by the high correlation coefficient ($r^2 > 0.99$) existing between the average CT density and the concentrations of tagging agent (KBr in this example) in various brine samples (fig. 3). This range of concentrations is representative of the values encountered in a coreflood. Various concentrations of KBr, KI, NaBr, NaI could be used as tagging agents for the brine. The bromide compounds, although possessing lower X-ray attenuation than the iodide compounds, have an aesthetic advantage over the iodide compounds of being nonstaining when exposed to air.

For calculation of porosities and saturations, successive scans have to be taken at precisely the same positions with the core dry, fully brine saturated, and partly saturated (during actual flood).

For a two-phase system (oil and brine) the porosity and the fluid saturations are obtained for each voxel by solving the system of linear equations:

$$x_a\phi + x_r(1-\phi) = x_{ar} \quad (1)$$

$$x_b\phi + x_r(1-\phi) = x_{br} \quad (2)$$

$$(x_bS_b+x_oS_o)\phi+x_r(1-\phi)=x_{obr} \quad (3)$$

$$S_b+S_o = 1 \quad (4)$$

where

$x_a$ = CT density of air

$x_r$ = CT density of rock matrix

$x_{ar}$ = CT density of core (air & rock matrix)

$x_b$ = CT density of brine

$x_o$ = CT density of oil

$\phi$ = porosity

$S_b$ = brine saturation

$S_o$ = oil saturation

$x_{br}$ = CT density core fully saturated with brine

$x_{obr}$ = CT density core partly saturated with brine and oil

The above system has four unknowns: $S_b$, $S_o$, $\phi$, and $x_r$.

By eliminating $x_r$ from equations 1 and 2, one obtains the porosity $\phi$ which is substituted in equation 3 to yield $S_o$:

$$\phi = \frac{x_{br} - x_{ar}}{x_b - x_a} \quad (5)$$

$$S_o = \frac{x_{br} - x_{obr}}{(x_b - x_o)\phi} \quad (6)$$

$$S_b = 1 - S_o \quad (7)$$

For a relatively homogeneous sample, the porosity $\phi$ is relatively constant. Thus in equation 6, the denominator is also approximately constant, and the saturation variations $S_o$ and the flood front can be identified rapidly from the numerator by performing the image substraction operation available on the CT scanner between the core image during the flood ($x_{obr}$) and the image before the flood ($x_{br}$). The contrast between two saturation zones is shown in figure 4 where a 3-in.-long, 2 in.-diameter core previously saturated with oil and tagged brine is flooded with brine tagged with KBr (lighter grey) with the inlet port situated at the left. The location of the sudden change in the CT density, shown by the white curve, corresponds to the front location.

For a heterogeneous core, or if one wants to obtain correct porosity and saturation distributions, one has to use equations 5, 6, and 7 for each voxel. The core has to be first scanned dry ($x_{ar}$ values), fully saturated 100% with brine ($x_{br}$ values), and finally partially saturated during the flood ($X_{obr}$ value). The values of $x_a$, $x_b$, and $x_o$ are obtained from the scans of the coreholder filled with brine ($x_b$), with air ($x_a$) , or with oil ($x_o$).

Each of the scans (air, brine, oil, dry rock, rock with brine, and rock with oil) generates a 256 x 256 array of 2-byte elements. Generating the system of solutions 5, 6, and 7 for all the voxels requires transferring the image files from the CT to either a Microvax or a PC-based image processing system. By setting the baud rate at 9,600 baud on the serial card DL11-W in the CT computer, the transfer time of one image has been reduced to 7 minutes. At present, the image files are transferred from the CT scanner in ASCII format. Each voxel is represented by two hexadecimal numbers, each consisting of eight ASCII characters. The image file is converted for further processing into a binary file format compatible with the PC-based image processing system. Further increase in the transfer rate and adding batch capability can be performed by upgrading the CT computer operating system, adding the KERMIT communication package to it and transferring the image files in binary format. This approach would reduce the file transfer to less than 1 min/image.

The processing of files downloaded from the CT scanner is facilitated by using a menu-driven interface which allows quick access of the programs to be used with these files: file conversion, porosity calculation, saturation calculation, false color, etc. The image processing system consists of a dual monitor 286 AT compatible system with 3 MB RAM and a 80MB hard disk using the latest version of the American Inovision™ image processing hardware and software. The porosity and saturation distributions are written in file formats compatible with the image processing system for image analysis measurements. A pseudo color program can be used to attach selected colors to various ranges of porosity and saturation values. This allows differentiation of variations of porosity or saturations which in certain cases would be difficult to differentiate in the black and white display of various gray levels.

## Measurement of Fluid Distributions by CT Scanning

Effects of heterogeneities on fluid flow and oil trapping were first studied by performing waterfloods on a 10 cm x 5 cm x 2 cm slab of heterogeneous Shannon sandstone (fig. 5). On the CT scan of the dry slab, layers of higher porosity and permeability (darker colors), layers of lower porosity and permeability (lighter colors) and iron rich nodules (white spots) are observed. At the lower part of the sample the lighter coloring indicates tighter rock plus shale streaks. These heterogeneities control the front fingering both during the drainage process (oil displacing the brine) and imbibition (brine displacing oil) process.

Figure 6 shows four progressive steps during a flood in which brine (white) displaces mineral oil tagged with 40% 1-bromododecane (black). The flood progresses sequentially from the upper left to the lower right, with injection port at left of each image. One can observe the effect of various rock permeabilities on the front advancement. The viscosities of the brine and the mineral oil were 1.006 and 30 cP, respectively. The four images represent (from top left to lower right) a succession of 0.09, 0.16, 0.22, 0.28 pore volume brine injected. The respective elapsed times from the start of the flood were 735, 1,035, 1,335, and 1,635 seconds. This corresponds to a front advancement speed of approximately 17 ft/d.

The volumetric monitoring of the oil and brine produced allowed the computation of average oil and brine saturations during the flood. The average saturations calculated from CT scans agreed within 1% with those calculated from volumetric measurements (table 1).

Gas-liquid flow behavior was studied during the drying of the core. The core saturated with isopropyl alcohol (IPA), was dried with nitrogen gas. Two distinct stages of IPA saturation distributions have been observed in the CT scans. In the first stage, (figs. 7a and 7b) fingering controlled by rock heterogeneity reaches the outlet almost instantaneously. Injected $N_2$ gas preferentially flows through the center, more porous region, and avoids the tight outer region. The region behind the front (white) represents saturations in the 50 to 80% range while ahead of the front (gray) the rock is fully saturated (100%) with IPA. In the second stage, another front appears (figs. 7c and 7d) with the fingering of the front not as pronounced as previously, but nevertheless also controlled by rock heterogeneity. The region behind this front (black) is dry rock, while ahead of it is partially saturated. The images (from top left to bottom right) have been taken at 3, 150, 3,000 and 4,800 seconds from the beginning of the nitrogen flow. After 3 hours of flow, the average IPA saturation in the rock was reduced to 2%. The core was completely dry after allowing the gas flow overnight, with a total of $3 \times 10^6$ $cm^3$ of nitrogen having flowed through the system.

## Coreflood Experimental Results

The effects of lamination type heterogeneities on fluid distribution were studied by CT, NMR, and micromodels for two extreme cases: one for low porosity and permeability contrast between the laminations and one for high contrast. For the low contrast case, Berea rock was selected. The high contrast rock selected was from the Shannon formation. The porosity and permeability of the laminations were determined by using petrographic image analysis methods described previously.[3] Sixty images were captured for each of the two thin sections by using a 10x objective for the Berea and 5x objective for Shannon. Average values for the cores, based on image analysis, agree well with values determined by routine core analysis (table 2).

Because of the high permeability of the heterogeneous rocks selected (see the section on petrographic analysis), the corefloods could be performed at low differential pressures. Therefore, it was more experimentally convenient to cut slabs 2 x 5 x 3/4 in. and encapsulate them in Castolite™ clear resin. The Berea slab was cut with laminations at a 45° angle with respect to the direction of flow. The Shannon slab was cut with the laminations parallel to the flow direction. CT scans of both porosity and saturation distributions during drainage and imbibition processes for slabs are shown in figures 8, 9, and 10. The porosity and saturation distributions were obtained by following the procedures described in the "Porosity and Saturation Calculations" section after downloading the necessary files from the PDP 11-34 computer which is part of CT to the AT computer, on which the calculations and image display are performed. Both miscible (synthetic brine tagged with 5% NaI displacing untagged brine) and immiscible processes (drainage-imbibition cycles) of tagged synthetic brine and untagged synthetic oils 6.5 and 20 cP viscosity were studied. In figures 9 and 10 the injection is from the left. The effects of laminations on the front movement and the brine and oil saturations are shown in figure 9 for the Berea slab. By monitoring pressures and flow rates, end point relative permeabilities have also been calculated. The low porosity/permeability contrasts laminations showed a pronounced effect on the front shape during the oil flood of the brine-saturated Berea slab (fig. 9). At the end of the oilflood, the difference in saturation between the higher and lower porosity Berea laminations was barely detectable.

During waterflood the effect of the laminations was to yield a pistonlike front (fig. 9b). After the waterflood (2 pV) the difference between the laminations was less than the experimental saturation resolution (5% saturation).

For the Shannon slab, the high-permeability porosity/permeability layers provided channels for the oil flow (fig. 10a), and at the end of the oil flood essentially no oil penetrated the low-permeability layers. During the waterflood, fingering effect was present along the low-porosity, high-water-saturation layers (fig. 10b). At the end of the waterflood, saturation differences between the high- and low-porosity layers were close to the experimental resolution. These investigations have been reported in more detail.[6]

## NUCLEAR MAGNETIC RESONANCE IMAGING

### Method Development

The work emphasis in NMRI was to adapt the JEOL NMR spectrometer for imaging at the regular high magnetic field (6.4 Tesla), thus ensuring a quick conversion from spectroscopy to imaging and creating the possibility to perform multinuclear high resolution imaging. Previous imaging was done at a lower magnetic field (1.43 Tesla) than that required for spectroscopy (6.4 T). The lower field was required due to the presence of a longer spin-spin relaxation time, $T_2$, for protons in porous media at low field

strengths. This longer relaxation time allows the use of 2D spin-echo NMRI techniques in which the sample is "sliced" successively. The files thus generated could be processed on the NMR spectrometer computer, and images corresponding to proton density distributions could be generated. This approach was found to have important limitations. First, it was time consuming to change the magnetic field of the spectrometer to the imager requirements and risked possible damage to the magnet. Second, at low magnetic fields, multinuclear detection as well as higher spatial resolution could not be achieved. Based on these findings, the magnetic field changes were eventually found to be unacceptable, and the decision was made to operate the NMRI accessories at the 6.4 T magnetic field used for spectroscopy.

The spin-spin relaxation time ($T_2$) controls the amount of time that usable NMR signals persist after the radio-frequency (RF) pulse. After about five $T_2$ periods, the measurable signal disappears. At a proton frequency of 270 MHz, corresponding to the 6.4 T magnetic field, the $T_2$ times of fluids in porous rock are reduced to the 0.2 to 1 msec range (the shorter times are for rock containing clays or other materials containing many magnetic species such as Fe or Mn). To use NMRI for imaging these samples will require RF pulse sequences which are shorter than 5 msec. This eliminates most pulse sequences which image a "slice" of the sample by using a spin-echo method with a selective RF pulse of narrow bandwidth which lasts several milliseconds. Also, the three X, Y, and Z gradients must be turned on and off sequentially which adds 5 to 6 millisec more to these sequences. A shielded gradient coil system was designed and built in the previous fiscal year to shorten the response time required. Recent calibration tests of the shielded coil system showed that a sufficient reduction in response time for imaging in porous rock with the 2D spin-echo "slice" technique could not be achieved.

A three-dimensional (3D) projection-reconstruction NMRI method does not require this rapid gradient response as the gradients are turned on and a short RF pulse having a broad bandwidth irradiates the sample in the presence of the gradient which is then turned off after the signal is acquired. The advantage is that the NMR signal is acquired immediately after the RF pulse (about 5 $\mu$ sec) so that a strong signal is available. The disadvantage is that the entire sample is iradiated at once, generating very large data files and requiring longer sampling times and larger data processing periods. The data initially were processed on the Microvax and required about 20 min CPU time for 32 x 32 x 32 pixels, while the data transfer to and from the Microvax by using a serial port at 2400 baud added another 20 min. Higher resolutions, such as 128 x 128 x 128 pixels, increase these times proportionally to the number of pixels. For an image data file acquired at 128 x 128 x 128 pixel resolution (16 Mbytes), the total turnaround time required has been as long as 40 hours. This long time was required because the program runs were made on the Microvax at the low-priority batch mode with the CPU time shared with other users. Using DECNET to commmunicate between the JEOL LSI11 computer and the Microvax could reduce the transfer time to minutes even for the larger files. The processing of higher resolution files still would involve

unacceptably, long times. Using a benchmark program (Sieve of Eratosthenes) on several types of computers, including the MICROVAX and a 386 type microcomputer, demonstrated that a 20-MHz 386 computer was 5 times faster than the Microvax even without sharing the VAX on batch priority. This indicates an improvement in data processing speed of 20 to 30 times by going to a dedicated 33-MHz 386 computer. Based on these findings a 33-MHz 386 IBM compatible microcomputer with a Weitek coprocessor was installed and has operated in a fully dedicated mode for processing the NMR data files. The total turnaround process time has been reduced to a few minutes for 32-pixel resolution images and a few hours for 128-pixel resolution images, representing a time reduction by a factor of 8 compared to the Microvax.

Implementation of the 3-D method on our system also required a method for sweeping the field gradient through one hemisphere of the sampled volume by sequentially applying the appropriate X, Y, and Z components of the gradient to the gradient coils while irradiating the sample and collecting the signals. As the JEOL spectrometer is not set up to supply the needed sinusoidally varying gradient signals, an outside computer (a PC/XT compatible) was used. A digital-to-analog (DAC) board having four channels was installed, and software was written to send the three gradient components in sequence to the board which outputs an analog voltage that is amplified to produce the gradient currents for each component. A digital I/O board also was installed and has been used to detect the trigger signal from the spectrometer which turns the gradients on and off at the correct times in sequence with the RF pulse and signal acquisition. The software to drive this PC was written in Basic with a machine language subroutine to load the gradient components to the DAC board. This subroutine can update the three components in 30 $\mu$ sec, while the main basic program requires about 30 msec per cycle to read the trigger signal and call the subroutine. This response time appears to be adequate for image acquisition. A block diagram of the spectrometer/imaging system is shown in figure 11.

The approach to MRI microscopy using 3-D projection reconstruction is computer-intensive because of the large data files involved. Also, the experiments are time-consuming, particularly when deuterium images of residual water are collected in which several signals must be added to get adequate signal-noise ratios (the deuterium in $D_2O$ enables differentiation between the aqueous phase and the hydrocarbon phase). Therefore, the experiments necessarily must be static in nature. To go much beyond 128-pixel resolution would require a parallel processor computer system having several processors to speed computations and display. On the other hand, the projection reconstruction method has the advantage of the built-in parallel nature of the data processing thus permitting an easy transition to parallel processing.

With the developments in the 3D-reconstruction and image display software essentially complete, the NMRI work has first been focused on increasing the resolution of the system down to 25 $\mu$m on

samples prepared from polymer microspheres. These microspheres have a nominal size distribution of 100-500 μm diameter. Several beadpacks have been prepared and saturated with water using Teflon plugs inside a 15-mm NMR tube (12.5 mm ID) and a 4-mm tube (2.7 mm ID). Images of water between the microspheres of the 12.5 mm diameter beadpack with a resolution of about 120 microns have been acquired at 128 x 128 x 128 pixel resolution. The thickness of each slice is about 200 μm. Size-grading of the polymer microspheres revealed that the microspheres ranged from 130-900 μm actual diameter. The microspheres were sieved and graded into six size ranges: 750-900, 700-800, 530-700, 300-500, 200-350, and 130-250 μm. A small sample holder made of Teflon with a 2.7 mm ID has been used in constructing a beadpack using the 300-500 μm microspheres. One of the 128 slices showing the water distribution in the 2.7 mm beadpack with a resolution of 25 μm is shown in figure 12. The slice thickness is about 40 μm. The circular outlines of the microspheres are clearly evident, and the nearly uniform size of the graded microspheres (dark areas) is shown. The brighter areas represent higher water content.

## Experimental Results and Discussion From NMRI Imaging Studies

Samples of various types were contained in all-Teflon sample holders supported in 10-mm glass tubes to avoid proton signals from the holders. The beads or sand were packed inside the tubing section providing a sample about 8 mm long and 4.7 mm in diameter. For the Berea and Shannon sandstone samples, small cylindrical plugs 5 to 6 mm in diameter and 8 mm long were cut from bulk rock samples. Both rock plugs were selected to contain at least one visible lamination running along the axis of the cylinder (see section on petrographic analysis). Heat-shrink Teflon tubing formed a fairly tight-fitting container for the rock plugs. The samples in their holders were evacuated and saturated with 1% NaCl in 99.6% deuterium oxide ($D_2O$) as the aqueous phase. A deuterium MRI image of each sample was obtained. The resolution for the bead packs was 128 x 128 x 128, and that for the rock samples was 64 x 64 x 64. For the deuterium images of the packs, four signals at each gradient position were added to improve signal/noise ratio, while for the rock plugs eight signals were added. Images of the bead pack are much sharper from the higher resolution obtained. The beads were spherical and had a size range from 350 to 500 μm. The circular profile of individual beads is evident in the images.[7]

For the two-phase MRI experiments, Soltrol mineral oil (5-cP viscosity) was used as the oil phase. Red dye was used to color the oil phase to track its progress visually. For the packs, a syringe was used to push about 5 pore volumes of oil through the pack in about 10 minutes. The rock plugs were immersed vertically in the oil phase and centrifuged at 1,500 rpm for 4 hours to allow the oil phase to displace the aqueous phase. A proton MRI image was obtained for each sample to see the oil phase, and a second deuterium image was obtained without moving the sample to see the residual aqueous phase. The same respective resolutions were used as above for each sample. For the proton image, two signals were added at each gradient position with a 0.5-second interpulse delay and a 25-degree RF pulse. (The oil

had a longer spin-lattice relaxation time than the deuterium oxide.) Because the residual deuterium oxide was much less concentrated, 8 or 16 signals were added, respectively, for the packs or rock plugs to improve signal-noise ratios. Images of oil and brine distributions in the core plugs taken at a resolution of 64 x 64 x 64 pixels are shown in figures 13 and 14.

In the bead pack there are pore spaces where the aqueous phase was bypassed in some pore spaces during the displacement, leaving pockets of water in individual pore spaces. Also, the oil phase apparently displaced water preferentially in the outer perimeter of the pack leaving higher water content in the center of the pack nearer the bottom. For both the Shannon and Berea plugs, laminations were visible as zones with differentiated oil and water content. For clearer display of both oil and water simultaneously false color images have to be used.[1] This allows identification of the preferential zones for the two fluids.

The decision to display the rock images at a lower resolution than that of the bead pack was based on the respective properties of the NMR signals from the two types of samples. The fluids in the rock matrix had a natural NMR line width of 700 Hz for deuterium and 2,000 Hz for protons. For the polymer bead pack, the NMR line widths were 20 and 120 Hz, respectively, indicating that the higher displayed resolution was meaningful. Additional development, such as increasing the field gradients, could permit 20 micron of resolutions with MRI of rock/fluid systems, which would allow imaging of water/oil phases within pores instead of in a group of pores as now possible. Since many of these phenomena, as well as those observed in micromodel images, require color reproductions, the reader is referred to Mahmood et al.[7] which includes color photographic reproductions.

## MICROMODEL STUDY OF PORE LEVEL FLUID DISTRIBUTIONS

The experimental setup consisted of a modified geological microscope, a powerful fiber optic light source, a sensitive high-resolution monochromatic video camera (Plumbicon tube, 0.005 lux, 900 TV-lines), and a super-VHS VCR (450 lines). For photography, an automatic 35-mm camera was attached. Assembly[4] and experimental details[5] have been reported previously.

On the basis of a review of earlier research,[4-5] it seemed appropriate to use a layered rock sample and make thick sections of (2-3 mm) Berea and Shannon rock from which micromodels could be constructed with varying orientations of the layers. The focus of the micromodel flow experiments was to study the effect of layering on transient displacement behavior. A suitable layered rock slab was selected and CT-scanned to allow the cutting of thick sections (2-3 mm) without damaging layers.

The highest quality of observations and reproductions were possible for slow events spanning over 10s of minutes, such as foam degradation, emulsification, and interactions at rock/fluid interfaces. The

faster the events under observation, the lower the quality of reproductions became because of the low-light views. Quality was poor but acceptable for dynamic events occurring at moderate velocities (10 to 20 ft/d). Difficulties were observed when mass-reproducing events faster than this, such as foam formation, foam rupture, and most capillary-controlled phenomena. The quality of video recordings of these events was also marginal. For extremely difficult situations, direct observations through the microscope were used for interpretations.

The effect of dissimilarity in the wettabilities of the transparent silicon-rubber coating (preferentially oil-wet) and the rock grains could be important. However, the oil-wetting on the confining boundaries was manifested only after 10s of hours, which was enough duration to complete a test. On gas injection, however, the water films between oil and silicon rubber surfaces were broken, gradually causing an oil-wetting problem. Once this happened, the model had to be discarded because the process was irreversible.

The most serious concern one should have about any micromodel is the effect of neglecting scaling criteria. Satisfying them simultaneously at both macro- and microscopic levels is more difficult in micromodels than in core plugs because of the smaller overall dimensions of the sample. For example, if residual wetting phase saturation were 25% in a core plug, it would be much less in a micromodel made from a rock slab from the same core plug. In rock plugs, regions are unswept due to viscous by-passing. Because of smaller size, this by-passing is not identical in rock-slab micromodels. Further studies are needed to understand the true extent of this limitation.

Use of a 2- to 3-mm rock slab also introduces certain complexities in the observations. The flow is neither strictly two-dimensional as in network models, nor is it truly three-dimensional on a macroscale. Also, the pore-to-pore connection is lost for some pores adjoining the encapsulating (no-flow) boundaries. These factors limited the ability to visualize the entire network of pores, and fluid flow and trapping through selected pores which are strategically located were monitored. These limitations are not expected to alter the flow mechanism significantly.

Despite all the limitations described above, optical microscopy used with rock-slab micromodels is a viable tool, because it offers very good resolution down to micron level, permits dynamic imaging of slow/medium flow systems, and makes the investigation of rock/fluid interactions possible.

During oil (5-cP) injection into a brine-filled homogeneous Berea rock-slab model, fingering was clearly seen. Fingering was not evident in the layered Shannon rock-slab model because the heterogeneities diffused the fingers. Oil front advancement was rather layer-after-layer, i.e., the layer closest to the injection port was swept first, then the second layer, and so on. The tighter the layers, the

more the brine was held in them. Brine saturation was also higher near the producing end due to the end effects.

After secondary imbibition, i.e., after a cycle consisting of initial brine injection in dry rock, oil injection until brine production stops, and brine reinjection until oil production is stopped, most of the pores containing oil were almost completely filled with it, except in crevices and thin coatings of brine on the grain surfaces. Another common observation was the trapping of oil ganglia extending over several pores due to the viscous by-passing of displacing brine.

During gas injection into the oil-filled micromodel, gas propagated in the form of small isolated bubbles through oil-filled channels, thus producing oil. After the moveable oil was produced, gas then displaced brine.

Details of the micromodel studies and color images of oil, water, and gas distributions in both Berea and Shannon sandstones have been published.[7]

## PETROGRAPHIC ANALYSIS OF BEREA AND SHANNON SANDSTONES

Macroscopic examination of the Berea rock revealed a porous sandstone with only subtle layering seen in reflected light. The pores were discontinuous in the poorly defined "higher" porosity zones. The rock composition, based on visual scans of the thin section, includes: quartz 56%, feldspars 2%, rock fragments 10%, clay cement 3%, calcite cement 2%, heavy minerals 1%, and muscovite <1%. Diagenetic clays are not concentrated into beds or layers in this sample but are, instead, almost evenly distributed. Layering is not apparent within the thin section using the petrographic microscope. All that can be recognized are slightly more porous or slightly less porous areas that tend to be elongated. Such areas cannot be traced in bands visually along the known bedding direction, and they are discontinuous.

The porosity and permeability contrasts for the two slabs are summarized in table 2. One potential method for determining more or less porous zones is to count the number of contacts a given grain has with adjacent framework grains (contact index). In the Berea sample, the contact index in more porous areas (average 3.5 contacts per grain) is significantly different from that in less porous areas (average 5.4 contacts per grain). These results tend to reflect differences in packing of grains within the sandstone. Layering of porosity in this sample has been determined statistically by using the petrographic image analysis system developed previously at NIPER.[3] The porosity contrast between laminations ranges between 16 and 25% as determined by image analysis of thin section and 17 and 19% as determined from CT measurements.[6]

Macroscopic examination of the Shannon rock revealed a porous sandstone with cross laminations readily apparent in transmitted or reflected light. Cross laminae are visually enhanced by

brown coloration which contrasts with the blue-dyed epoxy of the more highly porous layers. The rock composition based on visual scan of the thin section includes: quartz 22%, chert 4%, feldspars 15%, rock fragments 2%, glauconite 25%, clay cement 1%, and micas 1%. The most characteristic feature of this rock sample is the abundance of rounded to compacted glauconite grains, which are the source of the brown to greenish brown coloration of some layers. Layering in this sample is created by the contrast of highly compacted glauconitic laminae with less compacted, less glauconitic, more porous laminae. Glauconite grains are soft and easily compacted between more rigid framework grains such as quartz, chert, or feldspar. The contact index within compacted, glauconite-rich laminae averages 5.8 but only 4.0 in the more porous, glauconite-poor laminae. Another difference between the two types of laminae is that the pores are much larger (average 100 to 150 μm diameter) in the more porous laminae than in the compacted laminae (average 50 to 70 μm diameter). In addition, the compacted laminae have a significantly larger proportion of completely collapsed pores. The porosity of laminations ranges between 12 and 28% as determined by image analysis of thin sections and 21 and 28% as determined from CT measurements.[6]

The Shannon sample, in contrast to the Berea, has layering that is more visually apparent. "Grain dense" layers were created by compaction, particularly of glauconite, and the compacted laminae are more laterally continuous. In addition, the mineralogical composition and rock types represented by the two samples are quite different.

## RESULTS AND CONCLUSIONS

CT scanning, thin slab micromodels, NMR imaging, and thin section computerized image analysis have yielded complementary information regarding fluid flow and trapping in heterogeneous porous media at resolutions ranging from 1 to 500 μm. Permeability-porosity correlations from thin section image analysis and porosity distributions from CT scans enable mapping of the permeability distributions within cores. Additional conclusions are given below.

- When capillary forces dominate, i.e., at very low flow rates, heterogeneities in Berea and Shannon sandstones have a more pronounced effect on initial oil saturation distribution than on residual oil saturation after waterflooding . This is not unexpected, since in water-wet systems capillary forces will tend to hold water in smaller pores forcing oil into higher permeability regions that are swept by the injected water.

- Layers with moderate permeability contrast across the direction of flow, as was the case for the Berea slab experiments, reduced the front instabilities and resulted in a piston-like displacement during waterflood.

- For both the Berea and Shannon sandstone samples, porosities determined from CT scanning were in agreement with those measured by conventional core analysis and by computerized petrographic image analysis.

- Permeability-porosity correlations obtained from image analysis could be combined with porosity distributions from CT scanning to generate core permeability distributions that can be used for fluid flow predictions.

- Two presentations of results from this project were made this year at national symposia.[6,7]

Next year, the study of the effect of core heterogeneities on fluid movement and trapping will be monitored by CT scanning during core floods performed at higher pressures. The transfer and processing of data will be improved to make possible quick generating of 3D displays of porosity, permeability and saturation distributions. Also, methods to decrease the impact of ferromagnetic and paramagnetic species in rock on the resolution of NMRI will also be investigated, to allow more detailed imaging of pore shapes, pore topology and fluid distributions at pore level.

## ACKNOWLEDGMENTS

The authors wish to acknowledge the advice and guidance of Dr. Matt Honarpour and the constructive input from Dr. Min Tham of NIPER; the support of Bob Lemmon of the Bartlesville Project Office of the U.S. Department of Energy; and the financial support of the U.S. Department of Energy through Cooperative Agreement DE-FC22-83FE60149.

## REFERENCES

1. Morgan, Carslile Lee. Principles of Computed Tomography. University Park Press, 1983.

2. Wellington, S. L.,and H. J. Vinegar. X-Ray Computerized Tomography . J. Pet. Tech., Aug. 1987, pp. 885-898.

3. Tomutsa, L., and A. Brinkmeyer. Using Image Analysis To Determine Petrophysical Properties of Reservoir Rocks. Dept. of Energy Report No. NIPER-444, 1989.

4. Mahmood, S. and N. L. Maerefat. New Techniques of Pore-Scale Visualization of Fluids in Porous Media: The Effect of Pore Structure of Fluid Distribution. Dept. of Energy Report. No. NIPER-372, 1988.

5. Mahmood, S. M. Fluid Flow Behavior Through Rock-Slab Micromodels in Relation to Other Micromodels, Dept. of Energy Report No. NIPER-448, 1990.

6. Tomutsa, L., S. M. Mahmood, A. Brinkmeyer, and M. Honarpour. Application of Intergrated Pore to Core Image Analysis to Study Fluid Distribution in Reservoir Rocks. Pres. at 1990 SPE Ann. Tech. Conf. and Exhib., New Orleans, LA, Sept. 23-26, 1990. SPE paper 20478.

7. Mahmood, S. M., D. Doughty, L. Tomutsa, and M. Honarpour. Pore Level Fluid Imaging Using High Resolution Nuclear Magnetic Resonance Imaging in Thin Slab Micromodels. Pres. at the 1990 Ann. Technical Conf. of the Society of Core Analysts, Aug. 13-15, 1990, Dallas, TX. SCA paper 9024.

TABLE 1. - Average oil saturation changes during waterflooding, Shannon outcrop core

| Volumetric, values, % | CT values, % | Difference between CT-volumetric oil |
|---|---|---|
| 7.5 | 7.9 | 0.4 |
| 8.6 | 9.3 | 0.7 |
| 9.4 | 10.1 | 0.7 |
| 11.0 | 11.4 | 0.4 |
| 12.3 | 12.6 | 0.3 |
| 13.7 | 13.7 | 0.0 |
| 15.0 | 15.4 | 0.4 |
| 16.3 | 16.0 | 0.3 |
| 17.4 | 17.5 | 0.1 |
| 18.8 | 18.1 | -0.7 |
| 20.1 | 21.7 | 0.6 |
| 23.0 | 22.4 | -0.6 |
| 23.8 | 23.8 | 0.0 |
| 24.9 | 26.1 | 1.2 |

TABLE 2. - Porosity and permeability comparison of petrographic image analysis and core analysis of Berea and Shannon sandstones

| | Berea | | Shannon | |
|---|---|---|---|---|
| | PIA[1] | Core analysis | PIA[1] | Core analysis |
| | | POROSITY, % | | |
| Highest value | 31.0 | -- | 44.0 | -- |
| Lowest value | 10.0 | -- | 18.0 | -- |
| Average value | 19.0 | 18.7 | 26.0 | 27.2 |
| | | PERMEABILITY, md | | |
| Highest value | 2,170 | -- | 11,906 | -- |
| Lowest value | 8 | -- | 141 | -- |
| Average value | 294 | 300 | 1,070 | 980 |

[1]Petrographic image analysis.

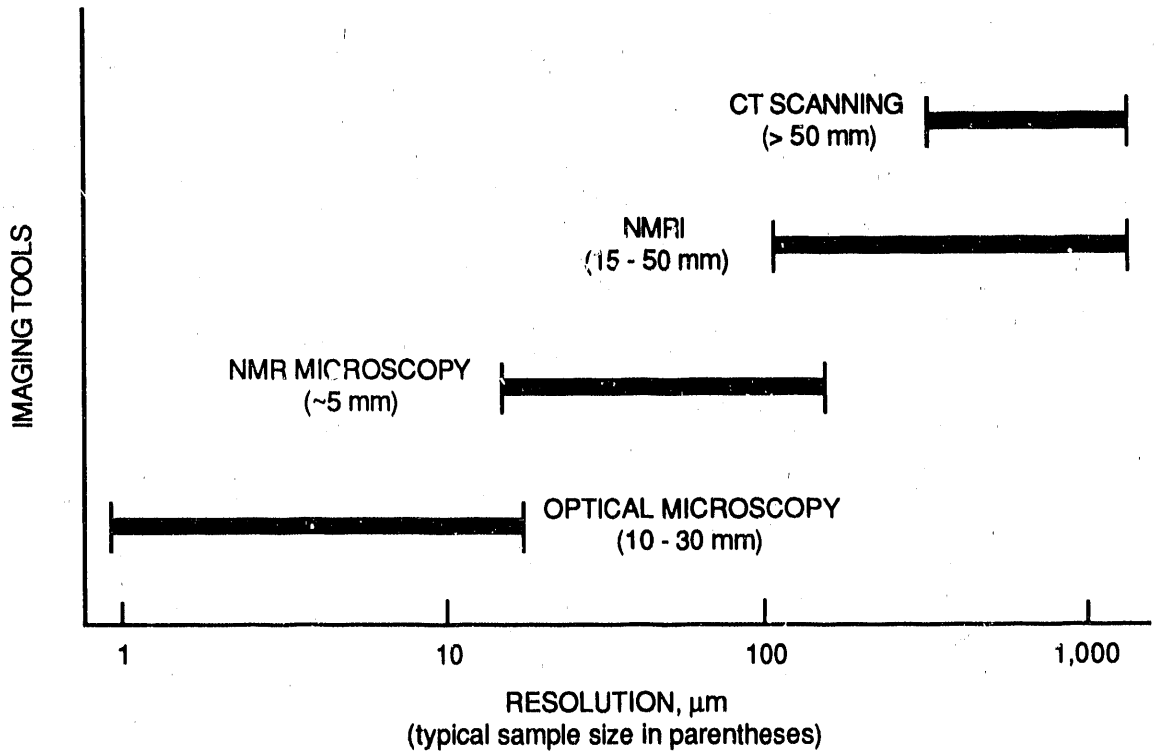


FIGURE 1. - Comparison of resolutions of various imaging techniques.

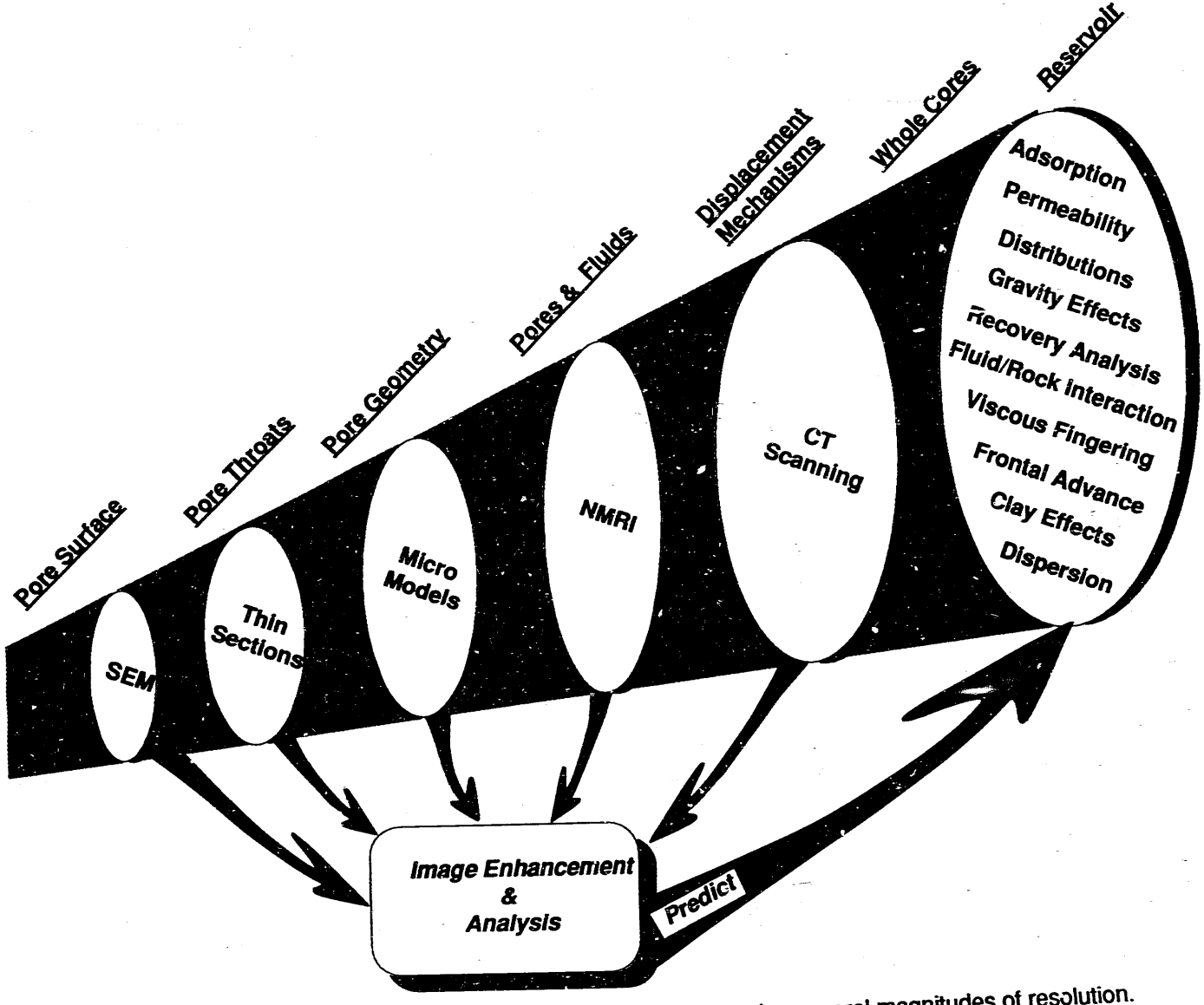


FIGURE 2. - Concept of integrating imaging technologies spanning several magnitudes of resolution.

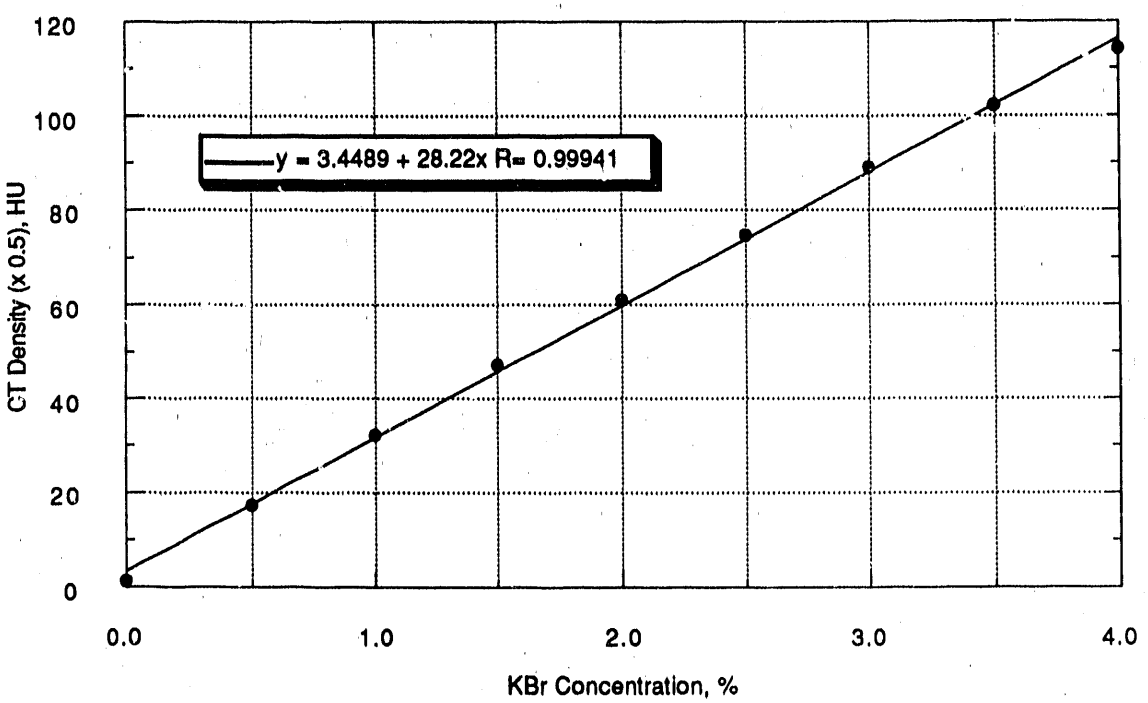


FIGURE 3. - X-ray attenuation vs. tagging agent concentration.

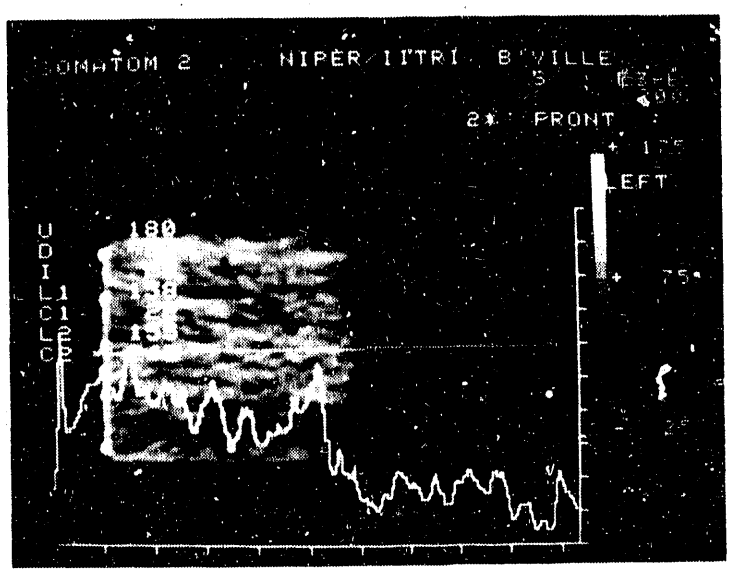


FIGURE 4. - Tagged brine (white) front movement in waterflood. Injection is from the left to the right. The white curve indicates the CT density and shows a sudden change at the fluid front.

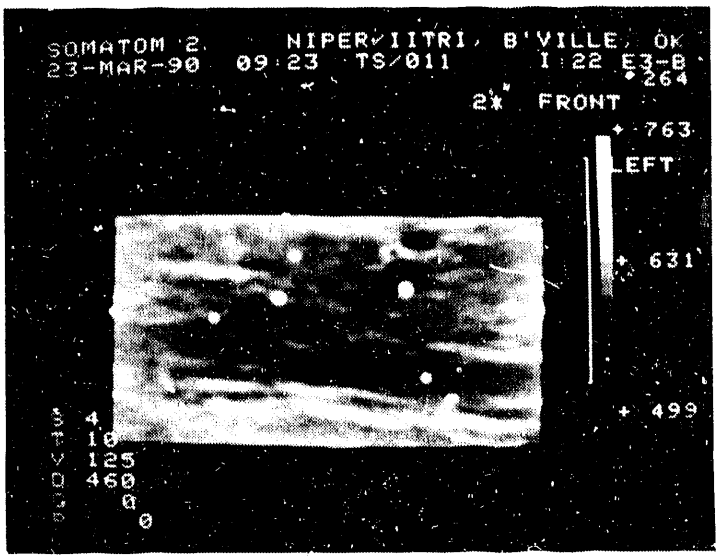


FIGURE 5. - CT scan of heterogeneous Shannon sandstone slab.

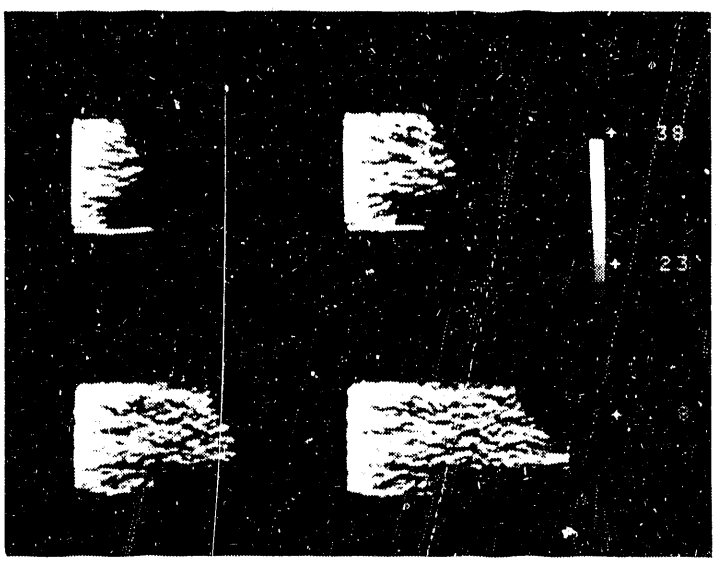


FIGURE 6. - Displacement of mineral oil (black) by brine (white).

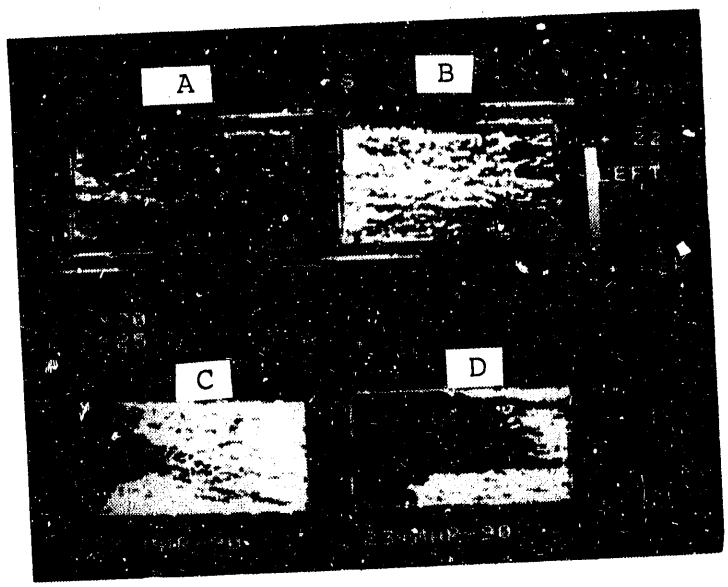


FIGURE 7. - Drying of Shannon sandstone slab saturated with isopropyl alcohol.

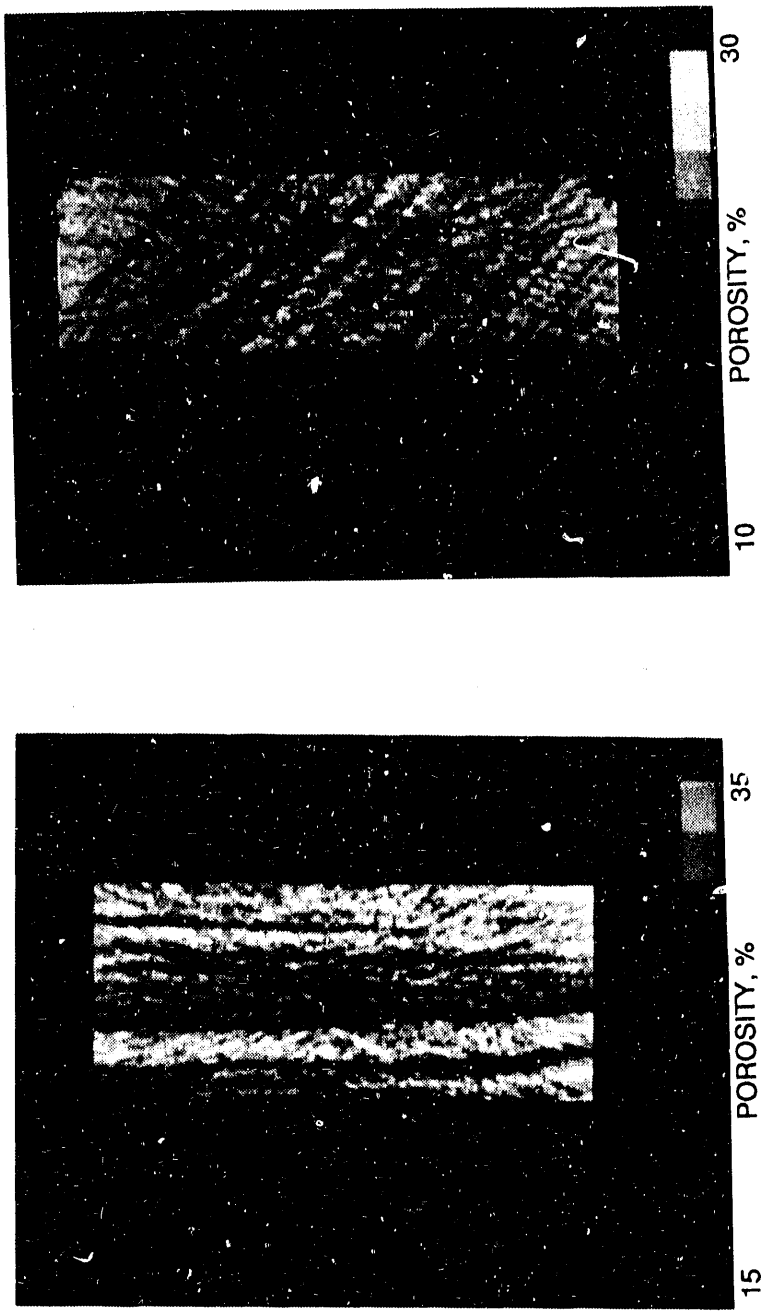


FIGURE 8. CT porosity distributions in (a) Berea and (b) Shannon slabs.

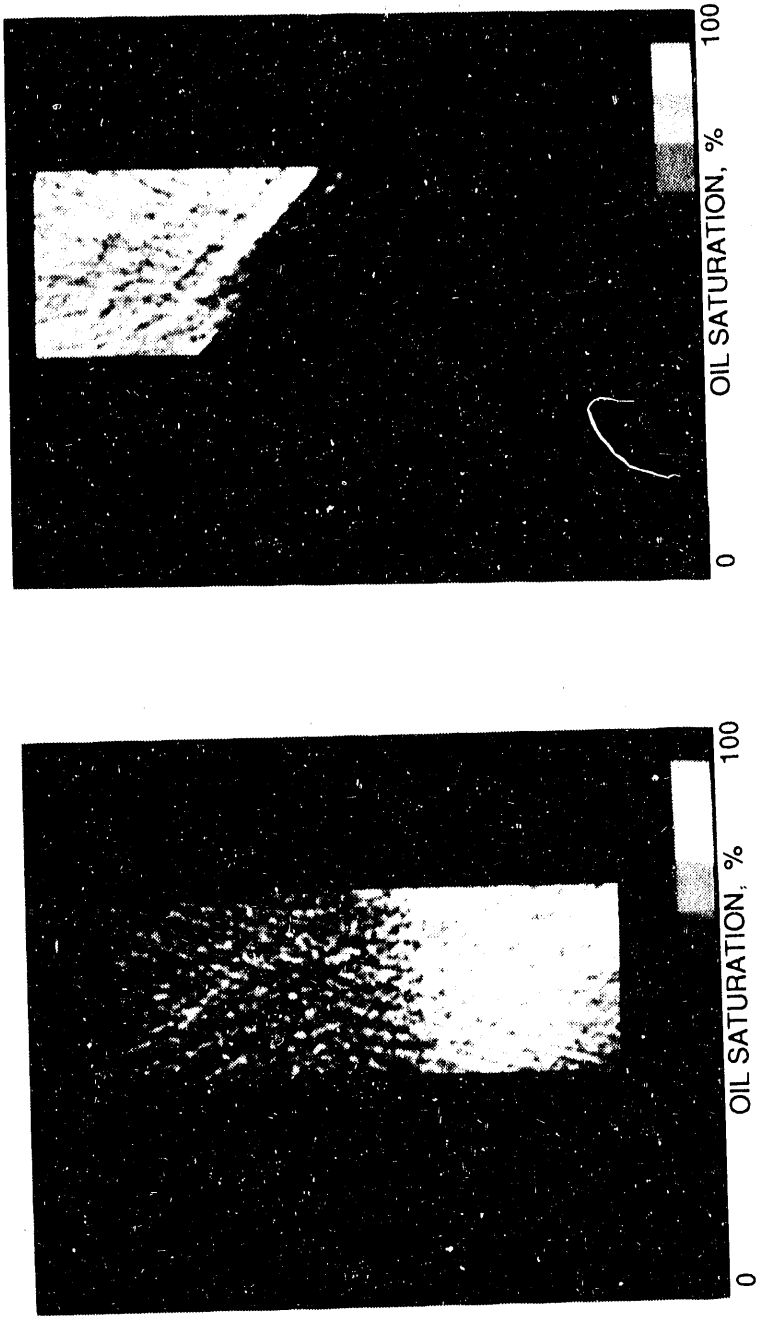


FIGURE 9. - Saturation distributions during (a) drainage and (b) imbibition process in a laminated Berea slab.

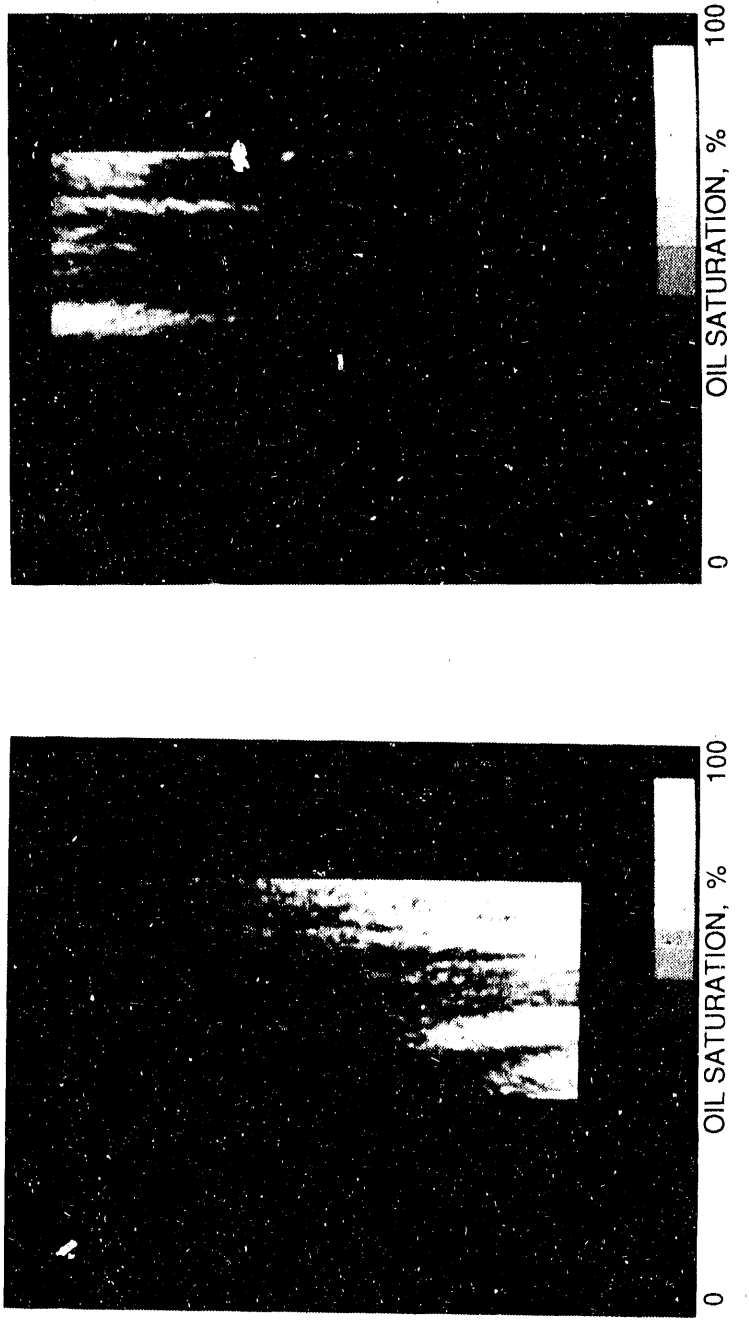


FIGURE 10. Saturation distributions during (a) drainage and (b) imbibition process in a layered Shannon slab.

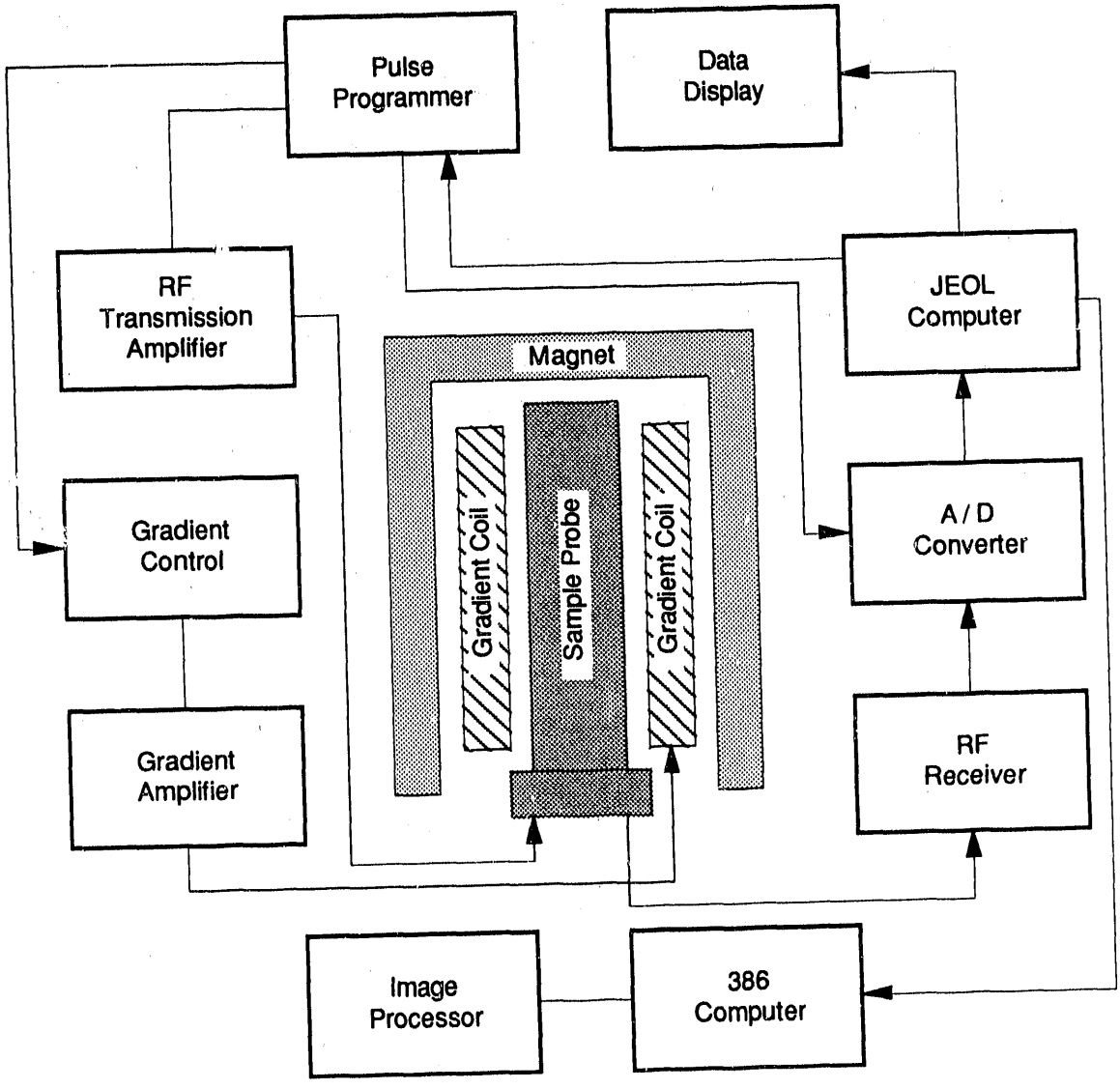


FIGURE 11. - Block diagram of NMRI system.

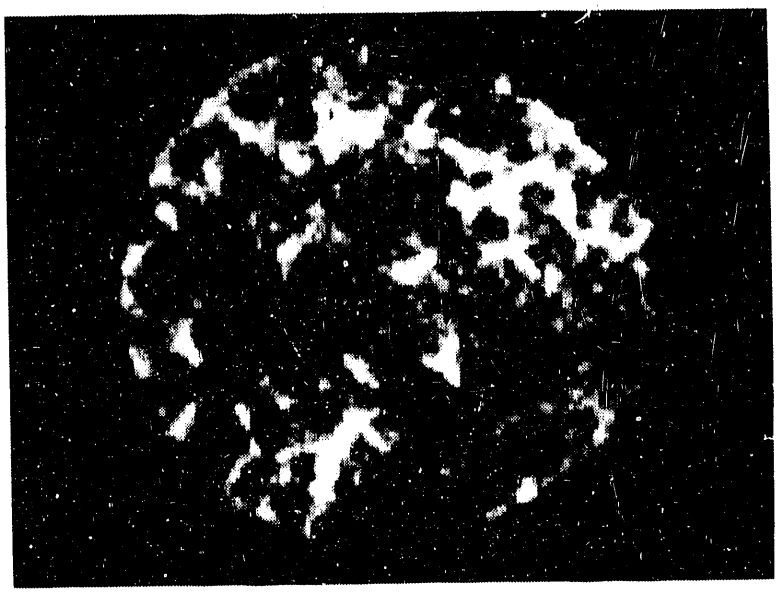

FIGURE 12. - High resolution NMRI image of water saturated beadpack.

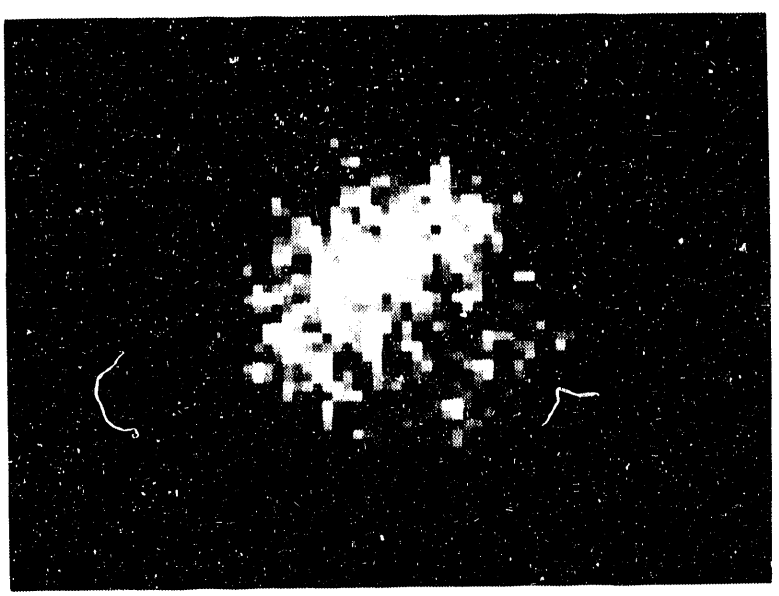

FIGURE 13. - Brine distribution, in the Shannon microplug.

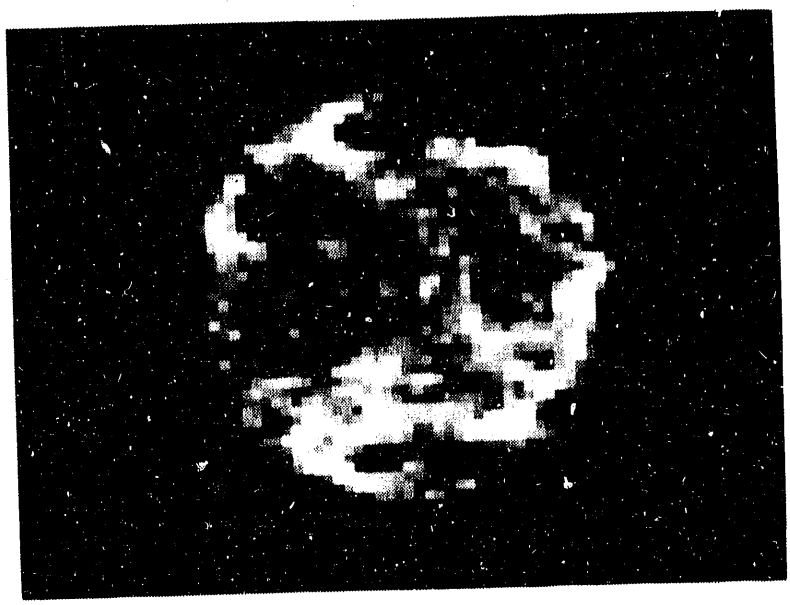

FIGURE 14. - Oil distribution in the Berea microplug.



★U.S. GOVERNMENT PRINTING OFFICE: 1990-561-02920061

# -END-

# DATE FILMED

02/27/91